



**HAL**  
open science

# Effect of upper- and lower-level baroclinicity on the persistence of the leading mode of midlatitude jet variability

Loïc Robert, Gwendal Rivière, Francis Codron

► **To cite this version:**

Loïc Robert, Gwendal Rivière, Francis Codron. Effect of upper- and lower-level baroclinicity on the persistence of the leading mode of midlatitude jet variability. *Journal of the Atmospheric Sciences*, 2019, 76 (1), pp.155-169. 10.1175/JAS-D-18-0010.1 . hal-01955765

**HAL Id: hal-01955765**

**<https://hal.sorbonne-universite.fr/hal-01955765>**

Submitted on 14 Dec 2018

**HAL** is a multi-disciplinary open access archive for the deposit and dissemination of scientific research documents, whether they are published or not. The documents may come from teaching and research institutions in France or abroad, or from public or private research centers.

L'archive ouverte pluridisciplinaire **HAL**, est destinée au dépôt et à la diffusion de documents scientifiques de niveau recherche, publiés ou non, émanant des établissements d'enseignement et de recherche français ou étrangers, des laboratoires publics ou privés.

1 **Effect of upper- and lower-level baroclinicity on the persistence of the**  
2 **leading mode of midlatitude jet variability**

3 Loïc Robert\* and Gwendal Rivière

4 *LMD/IPSL, Département de Géosciences, ENS, PSL Research University, École Polytechnique,*  
5 *Université Paris Saclay, Sorbonne Universités, UPMC Univ Paris 06, CNRS, Paris, France*

6 Francis Codron

7 *LOCEAN/IPSL, Sorbonne Universités, UPMC Univ Paris 06, CNRS, Paris, France*

8 \**Corresponding author address:* Laboratoire de Météorologie Dynamique, École Normale  
9 Supérieure, 24 rue Lhomond, 75005 Paris, France.

10 E-mail: lrobert@lmd.ens.fr

## ABSTRACT

11 The sensitivity of the variability of an eddy-driven jet to the upper- and  
12 lower-level baroclinicity of the mean state is analyzed using a three-level  
13 quasi-geostrophic model on the sphere. The model is forced by a relaxation in  
14 temperature to a steady, zonally symmetric profile with varying latitude and  
15 intensity of the maximum baroclinicity. The leading EOF of the zonally- and  
16 vertically-averaged zonal wind is characterized by a meridional shift of the  
17 eddy-driven jet. While changes in the upper-level baroclinicity have no signif-  
18 icant impact on the persistence of this leading EOF, an increase in lower-level  
19 baroclinicity leads to a reduced persistence. For small lower-level baroclin-  
20 icity, the leading EOF follows a classical zonal index regime, for which the  
21 meridional excursions of the zonal wind anomalies are maintained by a strong  
22 positive eddy feedback. For strong lower-level baroclinicity, the jet enters a  
23 poleward propagation regime, for which the eddy forcing continuously acts  
24 to push the jet poleward and prevents its maintenance at a fixed latitude. The  
25 enhanced poleward propagation when the lower-level baroclinicity increases  
26 is interpreted as resulting from the broader and weaker potential vorticity gra-  
27 dient which enables the waves to propagate equatorward and facilitates the  
28 poleward migration of the critical latitude. Finally, the decrease in EOF1 per-  
29 sistence as the lower-level baroclinicity increases is shown not to result from  
30 the impact of changes in the mean climatological jet latitude.

## 31 **1. Introduction**

32 Eddy-driven jets and storm tracks have a key role in mid-latitude surface weather and it is im-  
33 portant to understand how they might respond to climate change. Results from the CMIP project  
34 experiments show a robust poleward shift of the jet in the Southern Hemisphere (Kidston and Ger-  
35 ber 2010), but the picture is more complicated in the Northern Hemisphere ocean basins (Barnes  
36 and Polvani 2013; Simpson et al. 2014; Vallis et al. 2015). In particular, there are competing influ-  
37 ences of the local warming maxima in the upper tropical troposphere (Seager et al. 2003; Lu et al.  
38 2008) and near the surface in the Arctic (Oudar et al. 2017), which change the meridional temper-  
39 ature gradient in opposite directions at different levels in the vertical, and therefore have opposite  
40 effects in terms of jet shifts (Butler et al. 2010; Rivière 2011; Chavaillaz et al. 2013; Harvey et al.  
41 2014; Shaw et al. 2016).

42 A change of the mean jet latitude can change its variability; as the mean jet moves poleward, its  
43 leading mode of variability – usually characterized by a latitudinal wobbling – often becomes less  
44 persistent, possibly because of a weaker positive eddy feedback (Barnes et al. 2010; Kidston and  
45 Gerber 2010; Arakelian and Codron 2012, see Fig. 5e), even if some studies with comprehensive  
46 models suggest that this relationship may not be as robust as initially thought (Simpson et al.  
47 2013a; Simpson and Polvani 2016). Moreover, the dominant mode of variability may change its  
48 nature for high-latitude jets and become characterized more by a pulse in amplitude than by a  
49 latitudinal shift (Barnes and Hartmann 2011). The jet variability seems also strongly sensitive  
50 to the latitude of wave excitation, either the latitude of stochastic stirring in a barotropic model  
51 (Barnes et al. 2010) or that of oceanic fronts in aquaplanet General Circulation Models (GCMs)  
52 experiments (Michel and Rivière 2014; Ogawa et al. 2016). In these studies, the persistence of the

53 leading mode of variability decreases as the wave excitation zone is shifted poleward, in agreement  
54 with the sensitivity to the jet latitude.

55 The impacts on the jet variability of changes in the mean temperature gradient or baroclinicity  
56 have been comparatively less studied. Son and Lee (2005, 2006) performed sensitivity numerical  
57 experiments in a dry GCM by varying the tropical heating and high-latitude cooling rates of the  
58 radiative equilibrium temperature profile used to force their model. The intensity of the tropical  
59 heating controlled the strength of the subtropical jet while the high-latitude cooling largely de-  
60 termined the width and strength of the mid-latitude baroclinic zone. For large tropical heating  
61 and small polar cooling, a single jet appeared and the leading mode was a latitudinal wobbling of  
62 the jet (also referred to as the zonal index regime). In the opposite range of the parameter space  
63 (small tropical heating and large polar cooling), a double-jet structure emerged at upper levels and  
64 zonal wind anomalies tended to propagate poleward (also referred to as the poleward propagation  
65 regime). The interpretation mainly relied on the shape of the time-mean potential vorticity gra-  
66 dient (Lee et al. 2007; Son et al. 2008). When it is strong and sharp as in the first case (zonal  
67 index), waves are meridionally trapped and mainly converge momentum into the jet core, leading  
68 to a strong positive eddy feedback. When it is weak and broad as in the second (propagating)  
69 case, waves propagate more easily equatorward and push the jet poleward. Similar arguments will  
70 be used in the present study when analyzing the sensitivity of the jet variability to the strength  
71 of the baroclinicity using a quasi-geostrophic model on the sphere. It is important to underline  
72 that our numerical setup significantly differs from the previously cited studies as the subtropical  
73 jet is weak in our quasi-geostrophic framework. Also, the originality of the present paper lies in  
74 the distinction made between the effects of changes in lower-level and upper-level baroclinicity.  
75 Changes in the vertical structure of the baroclinicity are known to have an effect on jet position

76 (Butler et al. 2010; Rivière 2011) and eddy intensity (Held and O’Brien 1992; Yuval and Kaspi  
 77 2016) but its effect on the jet variability has not apparently been studied so far.

78 The idealized quasi-geostrophic model used in the present study has three vertical levels, which  
 79 is the minimal framework to separate the baroclinicity into lower- and upper-level components.  
 80 This model is thus well suited to study in particular the effect of opposite tendencies in lower-  
 81 and upper-level temperature gradients, as occurs in global warming scenarios (Held and O’Brien  
 82 1992; Rivière 2011). The model is described in section 2, together with the different experiments.  
 83 The results describing the changes in the jet variability and eddy feedbacks when modifying the  
 84 lower and upper-level baroclinicity are presented in section 3, together with a dynamical interpre-  
 85 tation and sensitivity experiments to check the robustness of the results. Concluding remarks are  
 86 provided in section 4.

## 87 **2. Model and diagnostics**

### 88 *a. Numerical model*

89 The model used is the dry quasi-geostrophic model on the sphere of Marshall and Molteni (1993)  
 90 at a T42 resolution. It has three pressure levels in the vertical at 200, 500 and 800 hPa. The model  
 91 is governed by the following equations for the quasigeostrophic potential vorticity (PV)  $q_i$  at levels  
 92  $i = 1, 2, 3$ :

$$\begin{aligned} \frac{\partial q_i}{\partial t} + J(\psi_i, q_i) &= S_i - D_i, \\ q_i &= f + \Delta \psi_i + \left( \frac{\psi_i - \psi_{i+1}}{R_i^2} - \frac{\psi_{i-1} - \psi_i}{R_{i-1}^2} \right), \end{aligned} \quad (1)$$

93 where  $\psi_i$  is the streamfunction ( $\psi_0 = \psi_1$  and  $\psi_4 = \psi_3$ ),  $R_i$  is the deformation radius between levels  
 94  $i$  and  $i + 1$ ,  $S_i - D_i$  the source and dissipative terms,  $\Delta$  denotes the Laplacian operator, and  $f =$   
 95  $2\Omega \sin(\varphi)$  the Coriolis parameter. The deformation radii are set to  $R_1 = 660$  km and  $R_2 = 400$  km  
 96 as in Rivière (2009) and Robert et al. (2017), hereafter RRC17.

97 Source and dissipative terms are the sum of three distinct contributions that can be expressed as:

$$\begin{aligned}
 S_1 - D_1 &= -c_H \nabla^8 (q_1 - f) + \frac{1}{\tau_{R1}} \frac{\psi_1 - \psi_2 - \tilde{\psi}_1 + \tilde{\psi}_2}{R_1^2}, \\
 S_2 - D_2 &= -c_H \nabla^8 (q_2 - f) - \frac{1}{\tau_{R1}} \frac{\psi_1 - \psi_2 - \tilde{\psi}_1 + \tilde{\psi}_2}{R_1^2} + \frac{1}{\tau_{R2}} \frac{\psi_2 - \psi_3 - \tilde{\psi}_2 + \tilde{\psi}_3}{R_2^2}, \\
 S_3 - D_3 &= -c_H \nabla^8 (q_3 - f) - \frac{1}{\tau_{R2}} \frac{\psi_2 - \psi_3 - \tilde{\psi}_2 + \tilde{\psi}_3}{R_2^2} - \frac{1}{\tau_E} \nabla^2 \psi_3.
 \end{aligned}$$

98 The first term on the right-hand-side (rhs) of the equation represents a scale-selective horizontal  
 99 diffusion such that the damping time scale of the shorter waves at T42 truncation is 0.02 days.

100 The next term on the rhs represents a Newtonian relaxation in temperature toward a fixed profile  
 101 (denoted with a tilde) using two timescales at the two interfaces. Finally, a linear drag with a  
 102 timescale of  $\tau_E = 3$  days is applied to the third level.

103 The restoration temperature profile is zonally-symmetric and in thermal wind balance with a  
 104 Gaussian zonal jet given by :

$$\tilde{u}_i(\lambda, \varphi) = U_i \exp\left(-\frac{(\varphi - \varphi_0)^2}{d\varphi^2}\right), \quad (2)$$

105 where  $\varphi_0 = 30^\circ\text{N}$ , and  $d\varphi = 20^\circ$  are the control values of the mean position and width of the jet.

106 Control values of the restoration wind amplitude  $U_i$  are set to  $U_1 = U_0$ ,  $U_2 = 0.5U_0$  and  $U_3 = 0.2U_0$

107 where  $U_0 = 50 \text{ m s}^{-1}$ . In the rest of the paper, we define the baroclinicity by the vertical shear

108 of the zonal wind divided by the radius of deformation at the interface because the static stability

109 is a constant at each interface. The upper-level (lower-level) baroclinicity refers to  $(u_1 - u_2)/R_1$

110 ( $(u_2 - u_3)/R_2$ ) and its restoration counterpart is  $(\tilde{u}_1 - \tilde{u}_2)/R_1$  ( $(\tilde{u}_2 - \tilde{u}_3)/R_2$ ). The simulations are

111 15 years long to ensure significant results and the first year is discarded before the analysis, as in

112 RRC17.

113 *b. Simulations*

114 Different series of simulations have been performed to investigate the impact of changes of the  
115 upper- and lower-level baroclinicity. These series are shown in Table 1. Experiments where the  
116 upper-level baroclinicity is varied (denoted as UB) are obtained by fixing the equilibrium lower-  
117 level wind amplitude  $U_2$  and  $U_3$  to their respective control values and varying  $U_1$  from  $0.8U_0$  to  
118  $1.2U_0$ , corresponding to an upper-level baroclinicity factor  $(U_1 - U_2)/U_0$  varying from 0.3 to 0.7.  
119 That means that there is a factor of about 2.3 between the smallest and greatest values of the  
120 upper-level vertical shear of the restoration zonal wind. Similarly, experiments where the lower-  
121 level baroclinicity changes are obtained by fixing  $U_1$  and  $U_2$  and varying  $U_3$  from  $0.3U_0$  to  $0.1U_0$ .  
122 This corresponds to a baroclinicity factor  $(U_2 - U_3)/U_0$  varying from 0.2 to 0.4 and a lower-level  
123 vertical shear varying by a factor of 2.

124 The study is mainly focused on sensitivity experiments for which the relaxation time scales are  
125 set to  $\tau_{R1} = \tau_{R2} = 25$  days. This enables a systematic comparison between the effects of changes in  
126 upper- and lower-level baroclinicity as the relaxation time scales are the same at the two interfaces.  
127 These series are hereafter denoted as UB25 and LB25. Another set of sensitivity experiments  
128 is made with different time scales at the upper and lower interfaces ( $\tau_{R1} = 40$  days and  $\tau_{R2} =$   
129 15 days), as used in RRC17, hereafter denoted as UB40 and LB40. Finally, a series of simulation  
130 JP25 with fixed baroclinicity but changes in the jet position  $\phi_0$  is run to help assess the respective  
131 impacts of changes in the baroclinicity and jet latitude.



### 132 **3. Results**

#### 133 *a. Time-mean versus restoration baroclinicity*

134 Changes in the baroclinicity of the restoration temperature field do not necessarily induce the  
135 same changes in the simulated climatology because of the dynamical adjustment. Figure 1 shows  
136 the climatological upper- and lower-level baroclinicity fields obtained for the UB25 and LB25  
137 experiments. An increase in the upper- or lower-level restoration baroclinicity indeed leads to an  
138 increase of the corresponding climatological mean baroclinicity, as shown in Figs. 1a and d. We  
139 note that the upper-level baroclinicity maxima differ by a factor of 2 between the extreme cases in  
140 UB25 (Fig. 1a), which is a bit less than the range of the restoration baroclinicity. There is however  
141 little impact on the lower-level baroclinicity, with only a slight decrease and shift toward the pole.

142 For the LB25 series, the climatological mean lower-level baroclinicity also fluctuates over a  
143 smaller range of maxima than the restoration baroclinicity (Fig. 1b); but unlike the UB25 case the  
144 increase in the lower-level baroclinicity in LB25 simulations leads to a decrease in the upper-level  
145 one. This change in upper-level baroclinicity is due to the fact that the upper-level wind does  
146 not change as the lower-level baroclinicity is increased, while the middle- and lower-level winds  
147 increase (not shown). The increase in both the lower- and middle-level winds can be interpreted  
148 as follows. When the lower-level baroclinicity is increased, eddy energy increases but as the  
149 dissipation is acting at the low-level only, the low-level wind must increase. This also leads to an  
150 increase in the middle-level wind because the forcing is such that the baroclinicity at the interface  
151 between the low- and middle-level increases. These opposite changes in the two baroclinicities  
152 need to be kept in mind while interpreting the results. Similar results are obtained for UB40 and  
153 LB40 (not shown).

154 *b. Persistence of the leading mode and eddy feedbacks*

155 Following Lorenz and Hartmann (2001) and RRC17, Empirical Orthogonal Functions (EOF)  
 156 of the zonally and vertically averaged zonal wind are computed for each simulation of UB25 and  
 157 LB25. The autocorrelation function of the principal component (PC) of the leading EOF, hereafter  
 158 named PC1 and EOF1, of each experiment is plotted in Fig. 2. As in RRC17, the autocorrelation  
 159 has systematically a shoulder shape marked by a fast decay rate during the first few days followed  
 160 by a slower decay rate at longer lags. On average, the e-folding time is around 20 days, which is  
 161 of the same order of the timescales of the Southern Hemisphere annular mode in comprehensive  
 162 models as they vary between 15 and 30 days during summer (Kidston and Gerber 2010; Arakelian  
 163 and Codron 2012). It is however larger than the observed ones, which are closer to 10 days e-  
 164 folding (Simpson et al. 2013b; Simpson and Polvani 2016), as is often the case in comprehensive  
 165 and idealized models. A change in upper-level baroclinicity does not seem to impact the EOF1  
 166 persistence very much (Fig. 2a); however an increase in the lower-level baroclinicity causes a  
 167 clear decrease in persistence (Fig. 2b). After 20 days, the PC1 autocorrelation for strong lower-  
 168 level baroclinicity ( $U_2 - U_3 \geq 0.34U_0$ ) drops to 0.25 on average, whereas for weak lower-level  
 169 baroclinicity ( $U_2 - U_3 \leq 0.26U_0$ ), it remains above 0.5.

170 The tendency of the vertically and zonally averaged zonal wind  $\langle [u] \rangle$  satisfies the following equa-  
 171 tion (RRC17):

$$\frac{\partial \langle [u] \rangle}{\partial t} = -\frac{1}{a \cos^2 \varphi} \frac{\partial}{\partial \varphi} (\langle [u^* v^*] \rangle \cos^2 \varphi) - \frac{[u_3]}{3\tau_E}, \quad (3)$$

172 where  $u_3$  is the zonal wind in the lower level of the model, the operators  $\langle \rangle$  and  $[ ]$  correspond  
 173 to the vertical and zonal average respectively and  $u^* = u - [u]$  and  $v^* = v - [v]$  are departures of  
 174 the zonal and meridional wind from their zonal mean. The factor 1/3 in the second term of the  
 175 right-hand-side of Eq. (3) is due to the vertical integration of the momentum equation and the fact

176 that the Ekman dissipation is only acting in the lowest level. By projecting each term of Eq. (3)  
 177 onto EOF1, we get the tendency equation for PC1:

$$\frac{d\text{PC1}}{dt} = m + d, \quad (4)$$

178 where  $m$  is the eddy momentum forcing (i.e. the projection of the eddy momentum flux conver-  
 179 gence) and  $d$  is the projection of the surface drag. To get growth rates at a given time  $t$ , we compute  
 180 the time-lag cross-correlation between PC1 and each term of Eq. (4), then we divide them by the  
 181 autocorrelation function of PC1  $A_1(t_0) = \sum_t \text{PC1}(t)\text{PC1}(t_0 + t)$ :

$$\frac{1}{A_1} \frac{dA_1}{dt} = \frac{1}{\tau_m} + \frac{1}{\tau_d}. \quad (5)$$

182 where:

$$\tau_m^{-1}(t_0) = \frac{\sum_t \text{PC1}(t)m(t_0 + t)}{A_1(t_0)},$$

$$\tau_d^{-1}(t_0) = \frac{\sum_t \text{PC1}(t)d(t_0 + t)}{A_1(t_0)}.$$

183 The left-hand side of Eq. (5), which is the instantaneous rate of change of the PC1 autocorrela-  
 184 tion, is driven by two distinct contributions. On one hand,  $\tau_m^{-1}$  corresponds to the forcing due to  
 185 momentum flux convergence. On the other hand,  $\tau_d^{-1}$  corresponds to the effect of the drag. The  
 186 benefit of Eq. (5) is that  $\tau_d^{-1}$  is almost constant. Indeed,  $[u_3]$  is roughly proportional to  $\langle [u] \rangle$ , so  
 187 we expect  $d$  to evolve in line with PC1. Therefore, changes in the instantaneous rate of change  
 188 of the PC1 autocorrelation should mainly be caused by changes in the eddy momentum forcing  
 189  $\tau_m^{-1}$ . Figure 3 shows  $\tau_m^{-1}$  as a function of time lag and the baroclinicity factors  $(U_1 - U_2)/U_0$   
 190 and  $(U_2 - U_3)/U_0$ . In general, this quantity is very similar to the time-lag cross-covariance be-  
 191 tween PC1 and the eddy momentum forcing (i.e  $\sum_t \text{PC1}(t)m(t_0 + t)$ ). It exhibits strong positive  
 192 values at short negative lags which correspond to the triggering of the event by a strong pro-  
 193 jection of the convergence of eddy momentum onto the EOF. Then, at short positive lags it has  
 194 negative values in most cases. This was shown to come mainly from the negative feedback ex-

195 erted by planetary waves when they reflect on the flanks of the jet (Rivière et al. 2016, RRC17).  
 196 At longer positive lags, it usually reaches positive values due to a positive synoptic eddy feed-  
 197 back (e.g., Lorenz and Hartmann 2001, 2003; Zurita-Gotor 2014, RRC17). Even though the eddy  
 198 momentum contribution to  $A_{PC1}$  rate of change follows these different steps in most cases, dif-  
 199 ferences among the various cases exist and are worth analyzing. As expected from Fig. 2, the  
 200 values of the eddy momentum contribution shows almost no monotonic or consistent changes  
 201 when modifying the upper-level baroclinicity (Fig. 3a). One notable feature is the strong oscil-  
 202 lation for  $U_1 - U_2 = 0.6U_0$  which is probably due to successive wave reflections (Rivière et al.  
 203 2016, RRC17). Conversely, Fig. 3b shows a gradual increase in the eddy momentum contribution  
 204 at positive lags when the lower-level baroclinicity is decreased. At short positive lags (+2 to +3  
 205 days), the negative values found for large baroclinicity disappear and become positive for small  
 206 baroclinicity. At longer positive lags (+5 to +20 days), the eddy momentum contribution is near  
 207 zero for large baroclinicity and becomes positive for small baroclinicity.

208 Figure 4 compares each term of Eq. (5) for two extreme values of the lower-level baroclinicity.  
 209 As expected, the contribution of the drag is constant and similar for both simulations. For weak  
 210 lower-level baroclinicity (Fig. 4a), the eddy momentum contribution is significantly positive at  
 211 all positive lags. But for strong lower-level baroclinicity (Fig. 4b), it is first negative at short  
 212 positive lags, then becomes slightly positive between lag +5 and +12 days and finally decreases  
 213 and becomes again negative after lag +16 days. Hence, at all positive lags, the eddy momentum  
 214 contribution  $\tau_m^{-1}$  is stronger in the weak baroclinicity case.

215 Since the seminal work of Lorenz and Hartmann (2001), the positive correlation between  $m$   
 216 and PC1 at long positive lags (greater than 5 days) is considered as the signature of a positive  
 217 synoptic eddy feedback. Following this interpretation, the first main conclusion from Figs. 3 and 4  
 218 is that this positive feedback is weaker and less durable for stronger lower-level baroclinicity. The

219 second conclusion is that at short positive lags (less than 5 days), the negative feedback exerted by  
220 planetary waves as revealed in Rivière et al. (2016) and RRC17 becomes less effective for weak  
221 baroclinicity. These two changes go in the same direction, namely a decrease in persistence of the  
222 leading mode of jet variability with increased lower-level baroclinicity. The next section will be  
223 dedicated to investigate the underlying causes.

### 224 *c. Dynamical interpretation*

225 The aim of this section is to interpret the clear drop in PC1 persistence when the lower-level  
226 baroclinicity is increased. Fig. 5 shows the lagged regressions of the momentum flux conver-  
227 gence and zonal wind anomalies on PC1 for weak and strong lower-level baroclinicity. We first  
228 note that wind anomalies have more than three times higher amplitudes for stronger baroclinicity.  
229 This is logical as the lower-level baroclinicity largely determines the eddy growth rate (Lindzen  
230 and Farrell 1980; Hoskins and Valdes 1990) and so the higher amplitude of eddies for stronger  
231 baroclinicity lead to stronger momentum flux convergence and jet fluctuations. More interest-  
232 ingly, zonal wind anomalies propagate poleward for strong lower-level baroclinicity while they  
233 stay more or less at the same latitude for weak lower-level baroclinicity. For example, for the  
234 weak lower-level baroclinicity simulation, the maximum of negative wind anomalies (dashed con-  
235 tours on Fig. 5a) is around  $32^{\circ}\text{N}$  for a lag of -10 days and around  $34^{\circ}\text{N}$  for +20 days. In contrast,  
236 for a strong lower-level baroclinicity, the same anomalies peaks at  $35^{\circ}\text{N}$  for a lag of -10 days and  
237 around  $44^{\circ}\text{N}$  for +20 days. This difference can explain the eddy momentum contribution to  $A_{\text{PC1}}$   
238 rate of change seen on Fig. 4b. Indeed, the poleward-shifted zonal wind anomalies of Fig. 5b are  
239 due to poleward-shifted eddy momentum convergence patterns after lag +5 days which end up be-  
240 coming orthogonal to EOF1 due to its poleward propagation and can eventually project negatively  
241 onto it. Thus, the low or negative values of the cross covariance between  $m$  and PC1 in the strong

242 lower-level baroclinicity case correspond to a response of the eddies that does not maintain the jet  
243 shift associated with EOF1 but rather makes the jet propagate polewards.

244 The poleward propagation regime was found to emerge and dominate in the simulations of Son  
245 and Lee (2006), Lee et al. (2007) and Son et al. (2008) forced by a strong high-latitude cooling  
246 rate, that is when the mid-latitude baroclinic zone was reinforced and enlarged. This is consistent  
247 with our simulations which show the dominance of the poleward propagation regime when the  
248 mid-latitude lower-level baroclinicity is increased. The rationale for the poleward propagation  
249 regime provided by Lee et al. (2007) is the following :

- 250 • a wave generated in the jet core, which propagates equatorwards, induces momentum conver-  
251 gence near the jet core and a divergence on its equatorward flank.
- 252 • The momentum flux divergence decelerates the zonal wind near the critical latitude, which  
253 moves it poleward.
- 254 • The next equatorward propagating wave will therefore break slightly further away from the  
255 Equator, its momentum convergence and divergence patterns are shifted poleward compared  
256 to the first wave. Thereby, the jet is further pushed poleward and so on.

257 This mechanism needs the Rossby waves to reach a critical latitude on the equatorward flank  
258 of the jet and to strongly decelerate the westerlies there. This is unlikely to happen when waves  
259 do not propagate away from the jet and the jet somehow acts as a wave guide. This assertion  
260 can be tested by comparing the structure of Rossby waves between a weak and strong lower-level  
261 baroclinicity simulation. Figure 6 shows one point correlation maps of the meridional wind for  
262 both simulations with different lags : -2 days, 0 day and +2 days. On the one hand, the weak  
263 lower-level baroclinicity simulation (Fig. 6a, c and e) shows a prevalence of zonal wavenumber  
264  $k = 6$ . The waves are slightly anticyclonically tilted, as expected from spherical geometry and the

265 quasi-geostrophic model bias (Rivière 2009). Therefore, Rossby wave propagation is almost zonal,  
266 waves staying confined into the jet (compare Figs. 6a and e) which mainly acts as a waveguide.  
267 On the other hand, the strong lower-level baroclinicity simulation (Figs. 6b, d and f) is dominated  
268 by wavenumber  $k = 4$  and the observed wave structure has more pronounced tilts: a cyclonic tilt  
269 for the negative lag (Fig. 6b) and an even more pronounced anticyclonic tilt at the positive lag  
270 (Fig. 6f). At lag zero (Fig. 6d), waves seem to exhibit both tilts, cyclonic west from the reference  
271 point and anticyclonic east of it. This could indicate wave reflections occurring on the northern  
272 flank of the jet, which is consistent with the change in sign of the momentum flux convergence at  
273 short positive lags in Fig. 5b (Rivière et al. 2016). In any case, Fig. 6 reveals that waves tend to  
274 propagate more meridionally for the strong lower-level simulation. The stronger anticyclonic tilt  
275 observed there induces zonal wind deceleration on the equatorward side of the jet as needed in the  
276 above mechanism of poleward propagation.

277 This difference in wave structures can be related to the shape of the jet. Meridionally propagating  
278 waves are more likely to occur within broader jets for which the PV gradient is smoother and does  
279 not decrease too fast on the flanks of the jet while meridionally trapped waves are confined in well-  
280 defined regions of strong PV gradient (Martius et al. 2010). This picture is confirmed by Fig. 7  
281 which shows the time-mean zonal wind and PV gradient for LB25. The width of the jet increases  
282 while its peak amplitude stays roughly constant when the baroclinicity increases (Fig. 7a). For all  
283 simulations, the PV gradient has two peaks (Fig. 7b), a strong one located near the jet core and a  
284 weaker one closer to the Equator. The two peaks are stronger when the lower-level baroclinicity  
285 decreases and they also seem to be sharper. To confirm the latter statement, an estimation of the  
286 width at half maximum was computed for each simulation (Fig. 8c). It clearly shows a broader  
287 PV gradient as the lower-level baroclinicity increases. If the same computation is made for the  
288 UB25 simulations (Fig. 8a), the PV gradient is found to have a constant width, which supports our

289 interpretation and the fact that changes in upper-level baroclinicity does not influence the poleward  
290 propagation.

291 However, one may argue that the broader climatological mean jet and PV gradient is due to  
292 smearing by the larger meridional incursions when poleward propagation of zonal wind anoma-  
293 lies occur. It is thus not clear if a wider climatological mean jet necessarily means a wider jet  
294 at different times of the simulation. To address this issue, the width of the zonally-averaged PV  
295 gradient has been computed at each day of the simulations and then averaged. The result is shown  
296 in Fig. 8d (and Fig. 8b for UB25), which still clearly shows that the averaged width at half max-  
297 imum also increases with the lower-level baroclinicity and not with the upper-level baroclinicity.  
298 Therefore, a stronger lower-level baroclinicity leads to a broader jet and a smoother PV gradient,  
299 enabling the poleward propagation regime to become the dominant mode of variability. It confirms  
300 the interpretation provided by Lee et al. (2007) and Son et al. (2008). In their case, the poleward  
301 propagation regime associated with the broader and weaker PV gradient logically emerges when  
302 the baroclinic zone is forced to be broader by a stronger cooling rate at high latitudes. In our  
303 case, it is not straightforward to explain why the PV gradient and the jet broaden when the restora-  
304 tion baroclinicity is intensified and the meridional width of the restoration baroclinicity is kept  
305 unchanged.

306 Two possible mechanisms explaining how a stronger low-level (but not upper-level) baroclinicity  
307 leads to a broader jet can be put forward. The first one relies on baroclinic instability arguments.  
308 The development of baroclinic instability requires a change of sign of the PV gradient in the  
309 vertical; given that this gradient is always positive at upper levels, this is equivalent to having  
310 a negative PV gradient in the lower troposphere. An increase in lower-level baroclinicity will  
311 tend to enhance the negative low-level PV gradient, and therefore widen the latitudinal band in  
312 which it is negative, as shown in Figs. 9c and d for different restoration profiles (see Eq. (2)) for



313 their definition). In contrast, a change in upper-level baroclinicity does not affect the width of the  
314 region where the PV gradient changes sign in the vertical, as it remains positive at upper-levels  
315 (Figs. 9a and b). So, the latitudinal band in which baroclinic waves might be unstable increases in  
316 width only when the lower-level baroclinicity increases. This will in turn increase the width of the  
317 latitudinal band of eddy momentum deposition in the upper troposphere and thus the width of the  
318 eddy-driven jet.

319 The second potential explanation relies on changes in eddy wavelengths. There is a clear shift  
320 toward larger eddy lengthscales for stronger lower-level baroclinicity (compare Fig. 6 right and  
321 left columns). Figure 10 confirms it by showing the spectrum of the squared meridional wind as  
322 function of latitude and wavenumber for a weak and a strong lower-level baroclinicity simulation.  
323 This figure also confirms the assumption that waves are trapped in the jet for a weak lower-level  
324 baroclinicity (Fig. 10a), whereas they can escape and propagate meridionally for a stronger baro-  
325 clinicity (Fig. 10c). Moreover, waves tend to reach higher amplitudes for a stronger lower-level  
326 baroclinicity, and at all latitudes (compare Figs. 10b and d). The increase in eddy horizontal scale  
327 when the baroclinicity increases is consistent with similar quasi-geostrophic or primitive-equation  
328 simulations (Whitaker and Barcilon 1995; Chai and Vallis 2014). However, there are different  
329 competing mechanisms to explain this result and the mechanism at play may depend on the range  
330 of the baroclinicity (or criticality) values. One possible explanation might be the upscale nonlinear  
331 energy transfer. Indeed, an increase in the lower-level baroclinicity enhances wave generation of  
332 the most unstable synoptic waves. This intensifies non-linear interaction among synoptic waves  
333 that lead to more energy transfer toward large waves. There are also linear and alternative nonlin-  
334 ear arguments that may explain this result which are particularly more relevant when discussing  
335 weakly nonlinear regimes, as discussed in the two previously cited studies. So one possible in-  
336 terpretation for the broader jet in the presence of the stronger lower-level baroclinicity is the fol-

337 lowing: by increasing the baroclinicity, waves increase in scale so they deposit momentum over a  
338 broader region. This broadens the jet which in turn favors more the poleward propagation regime.  
339 We have checked that the upper-level baroclinicity has a less drastic effect on eddy length scales  
340 in the present simulations (not shown).

341 Finally, this shift towards smaller wavenumbers for strong lower-level baroclinicity could ex-  
342 plain another result: the stronger negative values of eddy momentum forcing at short positive lags  
343 observed (Fig. 3b). Smaller wavenumbers means more planetary waves which tend to reflect near  
344 the jet flank and induce a negative eddy momentum forcing (Rivière et al. 2016, RCC17). It could  
345 seem paradoxical that more reflections occur for strong lower-level baroclinicity when the jet acts  
346 less as a wave guide. However in that case, equatorward propagating planetary waves may reflect  
347 or be absorbed depending on the situation. The pronounced tilt observed on Fig. 6f (and to a lesser  
348 extent on Fig. 6d) is consistent with an increase in the wave-mean flow interaction described in  
349 Rivière et al. (2016), leading sometimes to the appearance of reflecting levels before the wave  
350 reaches the critical latitude. This well-marked equatorward wave propagation which may result in  
351 reflection or absorption does not appear for weak lower-level baroclinicity where waves are more  
352 systematically trapped in the jet core by the sharp PV gradient (Figs. 6c et e).

#### 353 *d. Additional sensitivity experiments*

##### 354 1) BAROCLINICITY INTENSITY VERSUS LATITUDE

355 As recalled in the introduction, changes in the persistence of the leading mode of jet variability  
356 have been linked to changes in the mean jet latitude (e.g., Kidston and Gerber 2010; Arakelian  
357 and Codron 2012) and one may argue that the results from the LB25 experiments could also be  
358 due to changes in the mean jet latitude. To check this, the LB25 series is compared to JP25, a  
359 series of simulations where the intensity of the restoration baroclinicity is fixed but its latitude is

360 varied. To compare these two series, we compute the instantaneous rate of change of the autocor-  
 361 relation function due to the eddy momentum forcing (term  $\tau_m^{-1}$  from Eq. (5)). Its averaged value  
 362 between lag +5 and +15 days is plotted on Fig. 11 for all simulations. We first recover in the  
 363 JP25 experiments the classical result (Barnes et al. 2010; Arakelian and Codron 2012) that as the  
 364 latitude of the mean jet increases, the eddy feedback coefficient decreases (black squares). The  
 365 LB25 experiments indicate that as the lower-level baroclinicity increases, the jet moves slightly  
 366 poleward, consistent with Butler et al. (2010) and Rivière (2011). For these experiments, the eddy  
 367 feedback also decreases as the jet moves poleward but with a much steeper slope than for the JP25  
 368 experiments. This strongly suggests that the impact of the lower-level baroclinicity onto the EOF1  
 369 persistence cannot be simply explained by the latitudinal displacement of the jet.

## 370 2) SENSITIVITY TO RELAXATION TIMESCALES

371 To check the robustness of the results, the same series of simulations as LB25 and UB25 has  
 372 been run but with the relaxation time scales set to the same values as in RRC17:  $\tau_{R1} = 40$  days  
 373 and  $\tau_{R2} = 15$  days. These setups, denoted as LB40 and UB40 (cf. Table 1), are also more similar  
 374 to the Held and Suarez (1994)'s benchmark. Figure 12 shows the PC1 autocorrelation for these  
 375 new series of simulations. As for LB25, the persistence of the leading EOF generally increases by  
 376 decreasing the lower-level baroclinicity while, as for UB25, this persistence is not impacted by a  
 377 change in upper-level baroclinicity. There is only one exception for the very weak baroclinicity  
 378 ( $(U_2 - U_3)/U_0$  equal to 0.20 and 0.22) for which the persistence suddenly decreases from 0.22  
 379 to 0.20. The general increased persistence as the baroclinicity decreases can be explained by  
 380 the increased eddy momentum forcing  $\tau_m^{-1}$  (Fig. 13b) as for the LB25 experiments. Only the  
 381 marginal cases for lower-level baroclinicity factors from 0.22 to 0.20 show an abrupt reversal of  
 382 the tendency. Similar to UB25, the eddy momentum forcing does not show significant change

383 in average when the upper-level baroclinicity is increased (Fig. 13a). In conclusion, the results  
384 found previously for  $\tau_{R1} = 25$  days and  $\tau_{R2} = 25$  days are still valid here, except for the very weak  
385 lower-level baroclinicity simulations.

#### 386 **4. Conclusions**

387 The impact of changes in upper- and lower-level baroclinicity on the eddy-driven jet variability  
388 has been investigated using a three-level quasigeostrophic model on the sphere. This study focused  
389 on the persistence of the leading EOF of the zonally- and vertically-averaged zonal wind. We  
390 found that its sensitivity to the upper or lower baroclinicity is very different: an increase in the  
391 upper-level baroclinicity has no significant effect whereas an increase in lower-level baroclinicity  
392 tends to decrease the EOF1 persistence.

393 When the lower-level baroclinicity increases, the EOF1 also becomes more characterized by a  
394 poleward propagation of zonal wind anomalies. Using the terminology introduced by Son and  
395 Lee (2006), the zonal index regime is progressively replaced by the poleward propagation regime.  
396 In the zonal index regime, the meridional excursion of the jet is maintained by a strong positive  
397 eddy feedback. In the poleward propagation regime, the eddies instead deposit their momentum  
398 poleward of the current jet position, leading to its propagation. The interpretation is provided in  
399 terms of PV gradient. For strong lower-level baroclinicity, the PV gradient is broad and weak  
400 enough to favor an equatorward propagation of the waves. Then, the waves decelerate the zonal  
401 winds on the equatorward flank of the jet when they break and displace the critical latitude further  
402 poleward. This tends to shift the eddy momentum flux convergence / divergence patterns and the  
403 zonal wind anomalies poleward with time. For weak lower-level baroclinicity, the PV gradient is  
404 so strong and sharp that the jet acts as a waveguide, waves are trapped and the deceleration of the  
405 zonal winds on the equatorward flank of the jet is too weak to modify the location of the critical

406 latitudes. The interpretation is similar to Lee et al. (2007) and Son et al. (2008) but the setup of  
407 the numerical experiments is different. In the previous studies, a broader PV gradient logically  
408 appears as the width of the forced baroclinic zone increases. In our case, an intensification of the  
409 restoration baroclinicity without changing its meridional width is enough to lead to the same effect.  
410 Two explanations are provided. The first one is based on a baroclinic instability argument. When  
411 the lower-level baroclinicity increases, the latitudinal band where baroclinic instability is likely to  
412 occur increases which enlarges the region of momentum deposit by the waves and hence widens  
413 the jet. The second one is based on the increased wavelength when the lower-level baroclinicity  
414 increases. As larger waves deposit momentum over a larger latitudinal band, the eddy-driven jet  
415 becomes broader.

416 Another effect of the increased wavelength when the lower-level baroclinicity increases is seen  
417 on shorter timescales. In the strong lower-level baroclinicity cases, the wave scale becomes larger  
418 and waves are more inclined to be reflected onto the equatorward side of the jet, reinforcing the  
419 negative eddy feedback a few days after the peak of PC1 (Rivière et al. 2016, RRC17). This consti-  
420 tutes an additional reason for the weaker persistence of PC1 for stronger lower-level baroclinicity.

421 The present idealized study provides dynamical diagnoses to further investigate the persistence  
422 of annular modes in future climate projections obtained with the CMIP (Climate Model Inter-  
423 comparison Project) exercises. In addition to the sensitivity to the jet latitude sensitivity already  
424 discussed in several papers (Kidston and Gerber 2010; Arakelian and Codron 2012; Barnes and  
425 Polvani 2013), the sensitivity to the lower-level baroclinicity and to the width of the PV gradient  
426 should be examined, especially during autumn and early winter when the polar amplification is  
427 expected to be the strongest in the Northern Hemisphere.

428 *Acknowledgments.* The authors would like to thank Jian Lu and two anonymous reviewers for  
429 their relevant and helpful remarks.

## 430 **References**

431 Arakelian, A., and F. Codron, 2012: Southern Hemisphere Jet Variability in the IPSL GCM at  
432 Varying Resolutions. *J. Atmos. Sci.*, **69**, 3788–3799, doi:10.1175/JAS-D-12-0119.1.

433 Barnes, E. A., and D. L. Hartmann, 2011: Rossby Wave Scales, Propagation, and the Variability  
434 of Eddy-Driven Jets. *J. Atmos. Sci.*, **68**, 2893–2908, doi:10.1175/JAS-D-11-039.1.

435 Barnes, E. A., D. L. Hartmann, D. M. W. Frierson, and J. Kidston, 2010: Effect of Latitude on the  
436 Persistence of Eddy-Driven Jets. *Geophys. Res. Lett.*, **37**, L11 804, doi:10.1029/2010GL043199.

437 Barnes, E. A., and L. M. Polvani, 2013: Response of the Midlatitude Jets, and of Their Variability,  
438 to Increased Greenhouse Gases in the CMIP5 Models. *J. Climate*, **26**, 7117–7135, doi:10.1175/  
439 JCLI-D-12-00536.1.

440 Butler, A. H., D. W. J. Thompson, and R. Heikes, 2010: The Steady-State Atmospheric Circulation  
441 Response to Climate Change-like Thermal Forcings in a Simple General Circulation Model. *J.*  
442 *Climate*, **23**, 3474–3496, doi:10.1175/2010JCLI3228.1.

443 Chai, J., and G. K. Vallis, 2014: The Role of Criticality on the Horizontal and Vertical Scales of Ex-  
444 tratropical Eddies in a Dry GCM. *J. Atmos. Sci.*, **71**, 2300–2318, doi:10.1175/JAS-D-13-0351.1.

445 Chavaillaz, Y., F. Codron, and M. Kageyama, 2013: Southern Westerlies in LGM and Future  
446 (RCP4.5) Climates. *Clim. Past*, **9**, 517–524, doi:10.5194/cp-9-517-2013.

- 447 Harvey, B. J., L. C. Shaffrey, and T. J. Woollings, 2014: Equator-to-Pole Temperature Differences  
448 and the Extra-Tropical Storm Track Responses of the CMIP5 Climate Models. *J. Atmos. Sci.*,  
449 **43**, 1171–1182, doi:10.1007/s00382-013-1883-9.
- 450 Held, I. M., and E. O’Brien, 1992: Quasigeostrophic Turbulence in a Three-Layer Model: Ef-  
451 fects of Vertical Structure in the Mean Shear. *J. Atmos. Sci.*, **48**, 1861–1870, doi:10.1175/  
452 1520-0469(1992)049<1861:QTIATL>2.2.CO;2.
- 453 Held, I. M., and M. J. Suarez, 1994: A Proposal for the Intercomparison of the Dynamical Cores  
454 of Atmospheric General Circulation Models. *Bull. Amer. Meteor. Soc.*, **75**, 1825–1830, doi:  
455 10.1175/1520-0477(1994)075<1825:APFTIO>2.0.CO;2.
- 456 Hoskins, B. J., and P. J. Valdes, 1990: On the Existence of Storm-Track. *J. Atmos. Sci.*, **47**, 1854–  
457 1864, doi:10.1175/1520-0469(1990)047<1854:OTEOST>2.0.CO;2.
- 458 Kidston, J., and E. P. Gerber, 2010: Intermodel Variability of the Poleward Shift of the Austral  
459 Jet Stream in the CMIP3 Integrations Linked to Biases in 20th Century Climatology. *Geophys.*  
460 *Res. Lett.*, **37**, L09708, doi:10.1029/2010GL042873.
- 461 Lee, S., S.-W. Son, K. Grise, and S. B. Feldstein, 2007: A Mechanism for the Poleward Propaga-  
462 tion of Zonal Mean Flow Anomalies. *J. Atmos. Sci.*, **64**, 849–868, doi:10.1175/JAS3861.1.
- 463 Lindzen, R. S., and B. Farrell, 1980: A Simple Approximate Result for the Maximum Growth  
464 Rate of Baroclinic Instabilities. *J. Atmos. Sci.*, **37**, 1648–1654, doi:10.1175/1520-0469(1980)  
465 037<1648:ASARFT>2.0.CO;2.
- 466 Lorenz, D. J., and D. L. Hartmann, 2001: Eddy-Zonal Flow Feedback in the Southern Hemisphere.  
467 *J. Atmos. Sci.*, **58**, 3312–3327, doi:10.1175/1520-0469(2001)058<3312:EZFFIT>2.0.CO;2.

- 468 Lorenz, D. J., and D. L. Hartmann, 2003: Eddy-Zonal Flow Feedback in the Northern Hemisphere  
469 Winter. *J. Climate*, **16**, 1212–1227, doi:10.1175/1520-0442(2003)16<1212:EFFITN>2.0.CO;2.
- 470 Lu, J., G. Chen, and D. M. W. Frierson, 2008: Response of the Zonal Mean Atmospheric  
471 Circulation to El Niño versus Global Warming. *J. Atmos. Sci.*, **21**, 5835–5851, doi:10.1175/  
472 2008JCLI2200.1.
- 473 Marshall, J., and F. Molteni, 1993: Toward a Dynamical Understanding of Planetary-Scale Flow  
474 Regimes. *J. Atmos. Sci.*, **50**, 1792–1818, doi:10.1175/1520-0469(1993)050<1792:TADUOP>2.  
475 0.CO;2.
- 476 Martius, O., C. Schwierz, and H. C. Davies, 2010: Tropopause-Level Waveguides. *J. Atmos. Sci.*,  
477 **67**, 866–879, doi:10.1175/2009JAS2995.1.
- 478 Michel, C., and G. Rivière, 2014: Sensitivity of the Position and Variability of the Eddy-Driven  
479 Jet to Different SST Profiles in an Aquaplanet General Circulation Model. *J. Atmos. Sci.*, **71**,  
480 349–371, doi:10.1175/JAS-D-13-074.1.
- 481 Ogawa, F., H. Nakamura, K. Nishii, T. Miyasaka, and A. Kuwano-Yoshida, 2016: Importance  
482 of Midlatitude Oceanic Frontal Zones for the Annular Mode Variability: Interbasin Differ-  
483 ences in the Southern Annular Mode Signature. *J. Climate*, **29**, 6179–6199, doi:10.1175/  
484 JCLI-D-15-0885.1.
- 485 Oudar, T., E. Sanchez-Gomez, F. Chauvin, J. Cattiaux, L. Terray, and C. Cassou, 2017: Respec-  
486 tive Roles of Direct GHG Radiative Forcing and Induced Arctic Sea Ice Loss on the Northern  
487 Hemisphere Atmospheric Circulation. *Climate Dyn.*, 1–21, doi:10.1007/s00382-017-3541-0.



- 488 Rivière, G., 2009: The Effect of Latitudinal Variations in Low-Level Baroclinicity on Eddy Life  
489 Cycles and Upper-Tropospheric Wave-Breaking Processes. *J. Atmos. Sci.*, **66**, 1569–1592, doi:  
490 10.1175/2008JAS2919.1.
- 491 Rivière, G., 2011: A Dynamical Interpretation of the Poleward Shift of the Jet Streams in Global  
492 Warming Scenarios. *J. Atmos. Sci.*, **68**, 1253–1272, doi:10.1175/2011JAS3641.1.
- 493 Rivière, G., L. Robert, and F. Codron, 2016: A Short-Term Negative Eddy Feedback on Mid-  
494 latitude Jet Variability due to Planetary Waves Reflections. *J. Atmos. Sci.*, **73**, 4311–4328, doi:  
495 10.1175/JAS-D-16-0079.1.
- 496 Robert, L., G. Rivière, and F. Codron, 2017: Positive and Negative Eddy Feedbacks Acting on  
497 Midlatitude Jet Variability in a Three-Level Quasigeostrophic Model. *J. Atmos. Sci.*, **74**, 1635–  
498 1649, doi:10.1175/JAS-D-16-0217.1.
- 499 Seager, R., N. Harnik, Y. Kushnir, W. A. Robinson, and J. A. Miller, 2003: Mechanisms  
500 of Hemispherically Symmetric Climate Variability. *J. Climate*, **16**, 2960–2978, doi:10.1175/  
501 1520-0442(2003)016<2960:MOHSCV>2.0.CO;2.
- 502 Shaw, T. A., and Coauthors, 2016: Storm Track Processes and the Opposing Influences of Climate  
503 Change. *Nature Geosc.*, **9**, 1965–1981, doi:10.1038/NGEO2783.
- 504 Simpson, I. R., P. Hitchcock, T. G. Shepherd, and J. F. Scinocca, 2013a: Southern Annular Mode  
505 Dynamics in Observations and Models. Part I: The Influence of Climatological Zonal Wind  
506 Biases in a Comprehensive GCM. *J. Climate*, **26**, 3953–3967, doi:10.1175/JCLI-D-12-00348.1.
- 507 Simpson, I. R., and L. M. Polvani, 2016: Revisiting the relationship between jet position, forced  
508 response, and annular mode variability in the southern midlatitudes. *Geophys. Res. Lett.*, **43**,  
509 2896–2903, doi:10.1002/2016GL067989.

- 510 Simpson, I. R., T. A. Shaw, and R. Seager, 2014: A Diagnosis of the Seasonally and Longitudinally  
511 Varying Midlatitude Circulation Response to Global Warming. *J. Atmos. Sci.*, **71**, 2489–2515,  
512 doi:10.1175/JAS-D-13-0325.1.
- 513 Simpson, I. R., T. G. Shepherd, P. Hitchcock, and J. F. Scinocca, 2013b: Southern Annular Mode  
514 Dynamics in Observations and Models. Part II: Eddy Feedbacks. *J. Climate*, **26**, 5220–5241,  
515 doi:10.1175/JCLI-D-12-00495.1.
- 516 Son, S.-W., and S. Lee, 2005: The Response of Westerly Jets to Thermal Driving in a Primitive  
517 Equation Model. *J. Atmos. Sci.*, **62**, 3741–3757, doi:10.1175/JAS3571.1.
- 518 Son, S.-W., and S. Lee, 2006: Preferred Modes of Variability and Their Relationship with Climate  
519 Change. *J. Climate*, **19**, 2063–2075, doi:10.1175/JCLI3705.1.
- 520 Son, S.-W., S. Lee, S. B. Feldstein, and J. E. T. Hovee, 2008: Time Scale and Feedback of Zonal-  
521 Mean-Flow Variability. *J. Atmos. Sci.*, **65**, 935–952, doi:10.1175/2007JAS2380.1.
- 522 Vallis, G. K., P. Zurita-Gotor, C. Cairns, and J. Kidston, 2015: Response of the Large-Scale Struc-  
523 ture of the Atmosphere to Global Warming. *Quart. J. Roy. Meteor. Soc.*, **141**, 1479–1501, doi:  
524 10.1002/qj.2456.
- 525 Whitaker, J. S., and A. Barcilon, 1995: Low-frequency Variability and Wavenumber Selec-  
526 tion in Models with Zonally Symmetric Forcing. *J. Atmos. Sci.*, **52**, 491–503, doi:10.1175/  
527 1520-0469(1995)052<0491:LFVAWS>2.0.CO;2.
- 528 Yuval, J., and Y. Kaspi, 2016: Eddy Activity Sensitivity to Changes in the Vertical Structure of  
529 Baroclinicity. *J. Atmos. Sci.*, **73**, 1709–1726, doi:10.1175/JAS-D-15-0128.1.
- 530 Zurita-Gotor, P., 2014: On the Sensitivity of Zonal-Index Persistence to Friction. *J. Atmos. Sci.*,  
531 **71**, 3788–3800, doi:10.1175/JAS-D-14-0067.1.

532 **LIST OF TABLES**

533 **Table 1.** Sensitivity experiment description table. . . . . 26

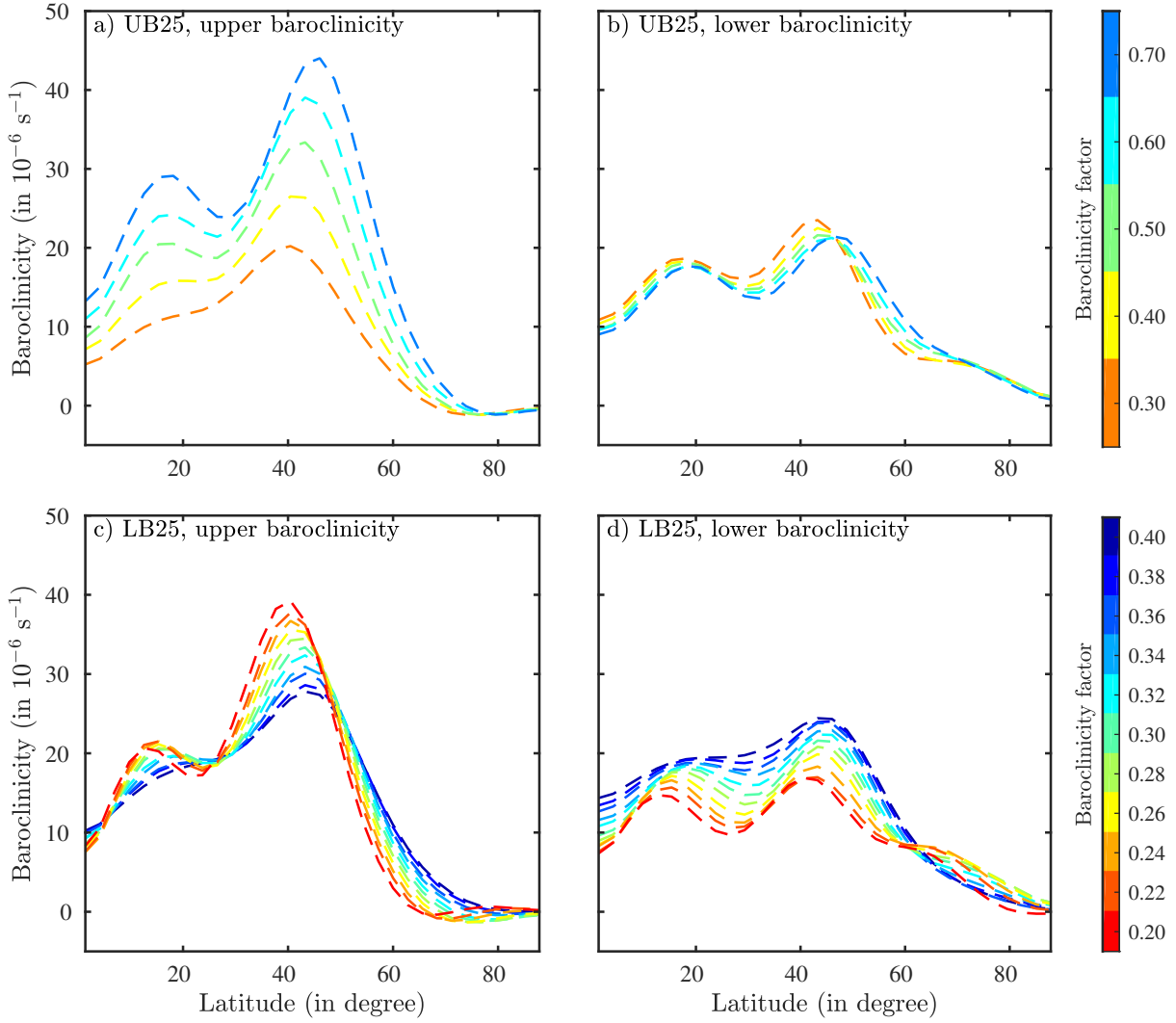
Name	$\tau_{R12}$	$\tau_{R23}$	Parameter	Minimum	Maximum	Step
JP25	25	25	$\varphi_0$	20°N	40°N	2°N
UB25	25	25	$U_1/U_0$	0.8	1.2	0.1
LB25	25	25	$U_3/U_0$	0.1	0.3	0.02
UB40	40	15	$U_1/U_0$	0.8	1.2	0.1
LB40	40	15	$U_3/U_0$	0.1	0.3	0.02

TABLE 1. Sensitivity experiment description table.

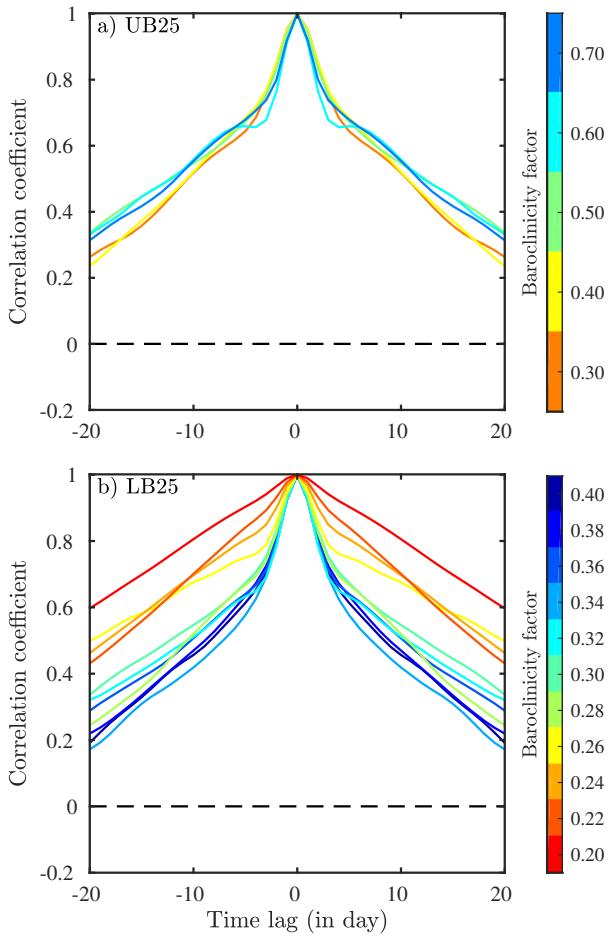
## LIST OF FIGURES

534		
535	<b>Fig. 1.</b>	Climatological mean of (left panels) upper- and (right panels) lower-level baroclinicity, respectively $(U_1 - U_2)$ and $(U_2 - U_3)$ , for (upper panels) UB25 and (lower panels) LB25. The baroclinicity factors correspond to $(U_1 - U_2)/U_0$ and $(U_2 - U_3)/U_0$ respectively. . . . . 29
536		
537		
538	<b>Fig. 2.</b>	Autocorrelation function of PC1 for (a) UB25 and (b) LB25 for which the baroclinicity factors are $(U_1 - U_2)/U_0$ and $(U_2 - U_3)/U_0$ respectively. . . . . 30
539		
540	<b>Fig. 3.</b>	eddy momentum contribution to the rate of change of the PC1 autocorrelation function ( $\tau_m^{-1}$ of Eq. (5)), as a function of lag and baroclinicity factors for (a) UB25 and (b) LB25. The baroclinicity factors in (a) and (b) correspond to $(U_1 - U_2)/U_0$ and $(U_2 - U_3)/U_0$ respectively. . . . . 31
541		
542		
543		
544	<b>Fig. 4.</b>	Rate of change of the PC1 autocorrelation function (left-hand-side of Eq. (5)), in green), and its momentum ( $\tau_m^{-1}$ of Eq. (5), in black) and drag contribution ( $\tau_m^{-1}$ of Eq. (5), in blue), for two simulations of LB25 : (a) weak baroclinicity ( $U_2 - U_3 = 0.2U_0$ ) and (b) strong baroclinicity ( $U_2 - U_3 = 0.4U_0$ ). . . . . 32
545		
546		
547		
548	<b>Fig. 5.</b>	Lagged regression onto PC1 of anomalous zonally and vertically-averaged eddy momentum flux convergence (in shading) and zonal wind (in contours, interval: $0.5 \text{ m s}^{-1}$ ) as a function of lag and latitude for two simulations of LB25 : (a) weak baroclinicity ( $U_2 - U_3 = 0.2U_0$ ) and (b) strong baroclinicity ( $U_2 - U_3 = 0.4U_0$ ). The black dashed-dotted lines indicate the meridional extension of the mean jet (taken as $\pm 10^\circ$ around jet maximum). . . . . 33
549		
550		
551		
552		
553	<b>Fig. 6.</b>	Lagged one point correlation map of the meridional wind for (left panels) weak lower-level baroclinicity ( $U_2 - U_3 = 0.2U_0$ ) and (right panels) strong lower-level baroclinicity ( $U_2 - U_3 = 0.4U_0$ ). These correlations maps have been plotted with a lag of (a,b) -2 days, (c,d) 0 day and (e,f) +2 days. The reference point, plotted using a white cross, is in each simulation close to the maximum of zonal wind. . . . . 34
554		
555		
556		
557		
558	<b>Fig. 7.</b>	Climatological mean of (a) the zonally averaged zonal wind and (b) zonally averaged PV gradient at 200hPa for LB25, the baroclinicity factor being $(U_2 - U_3)/U_0$ . . . . . 35
559		
560	<b>Fig. 8.</b>	(a,c) Full width at half maximum of the main peak of zonally averaged zonal wind (solid line) and PV gradient (dashed line) at 200hPa and (b,d) averaged full width at half maximum of the daily peak of the same quantities as a function of (a,b) the upper-level baroclinicity factor $(U_1 - U_2)/U_0$ for each simulation of UB25 and (c,d) the lower-level baroclinicity factor $(U_2 - U_3)/U_0$ for each simulation of LB25 (plotted with their respective color). . . . . 36
561		
562		
563		
564		
565	<b>Fig. 9.</b>	Vertical cross-section of the zonal wind (in shadings) and PV gradient (in contours, interval: $2 \cdot 10^{-11} \text{ m}^{-1} \text{ s}^{-1}$ ) of the restoration basic states for (a) weak upper-level baroclinicity ( $U_1 - U_2 = 0.4U_0$ ), (b) strong upper-level baroclinicity ( $U_1 - U_2 = 0.7U_0$ ), (c) weak lower-level baroclinicity ( $U_2 - U_3 = 0.2U_0$ ) and (d) strong lower-level baroclinicity ( $U_2 - U_3 = 0.4U_0$ ). . . . . 37
566		
567		
568		
569	<b>Fig. 10.</b>	(a,c) Spectrum of the squared meridional wind as a function of latitude and zonal wave number and (b,d) its integral over wavenumber for (a,b) a weak lower-level baroclinicity ( $U_2 - U_3 = 0.2U_0$ ) and (c,d) a strong lower-level baroclinicity ( $U_2 - U_3 = 0.4U_0$ ). . . . . 38
570		
571		
572	<b>Fig. 11.</b>	Feedback coefficient as a function of mean jet position for the JP25 series (in black squares) and the LB25 series (in colored diamonds), the baroclinicity factor being $(U_2 - U_3)/U_0$ . . . . . 39
573		
574	<b>Fig. 12.</b>	As Fig. 2 but for UB40 and LB40 series. . . . . 40

575 **Fig. 13.** As Fig. 3 but for UB40 and LB40 series. . . . . 41

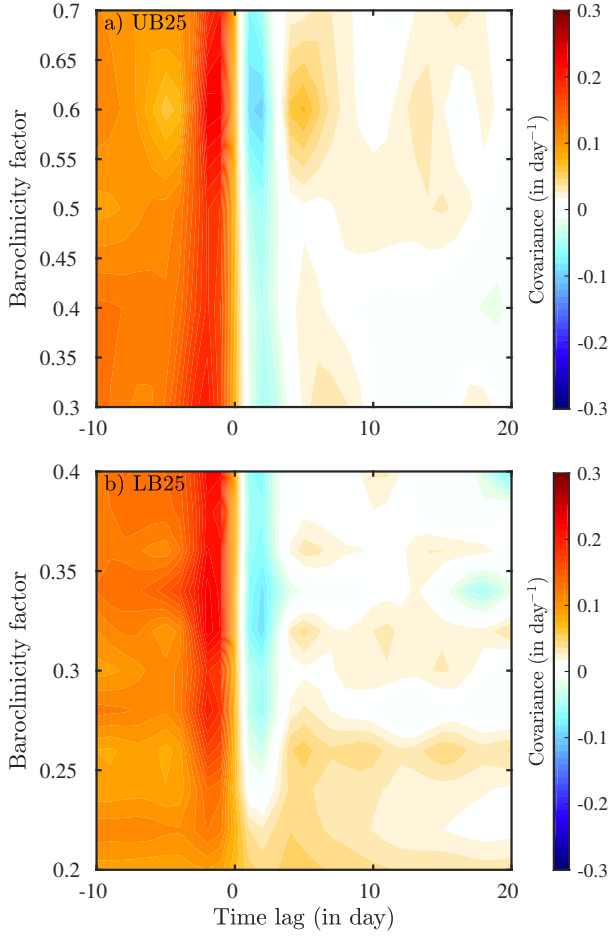


576 FIG. 1. Climatological mean of (left panels) upper- and (right panels) lower-level baroclinicity, respectively  
 577  $(U_1 - U_2)$  and  $(U_2 - U_3)$ , for (upper panels) UB25 and (lower panels) LB25. The baroclinicity factors correspond  
 578 to  $(U_1 - U_2)/U_0$  and  $(U_2 - U_3)/U_0$  respectively.

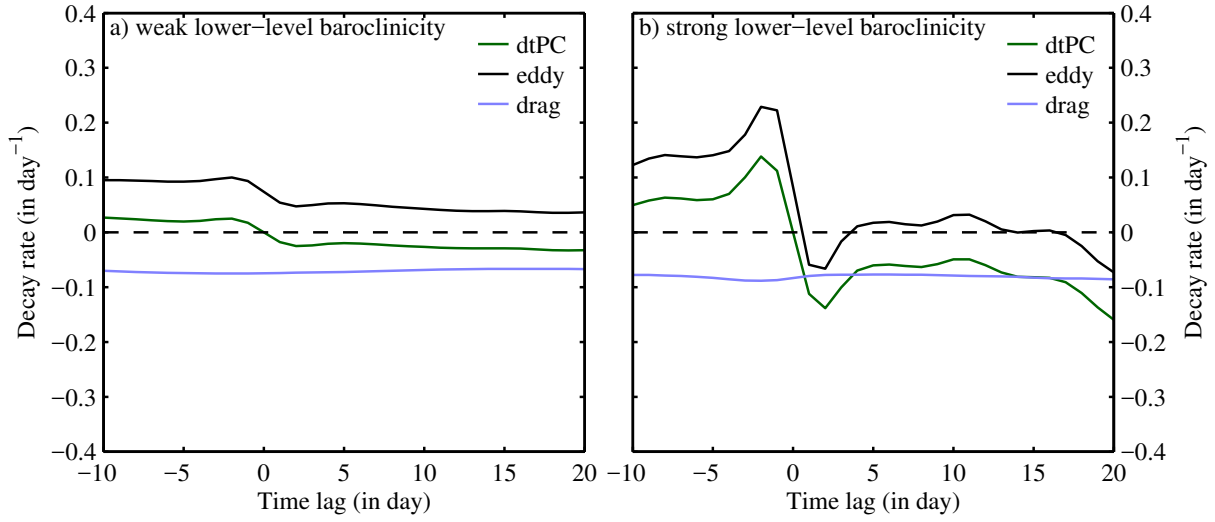


579 FIG. 2. Autocorrelation function of PC1 for (a) UB25 and (b) LB25 for which the baroclinicity factors are  
 580  $(U_1 - U_2)/U_0$  and  $(U_2 - U_3)/U_0$  respectively.

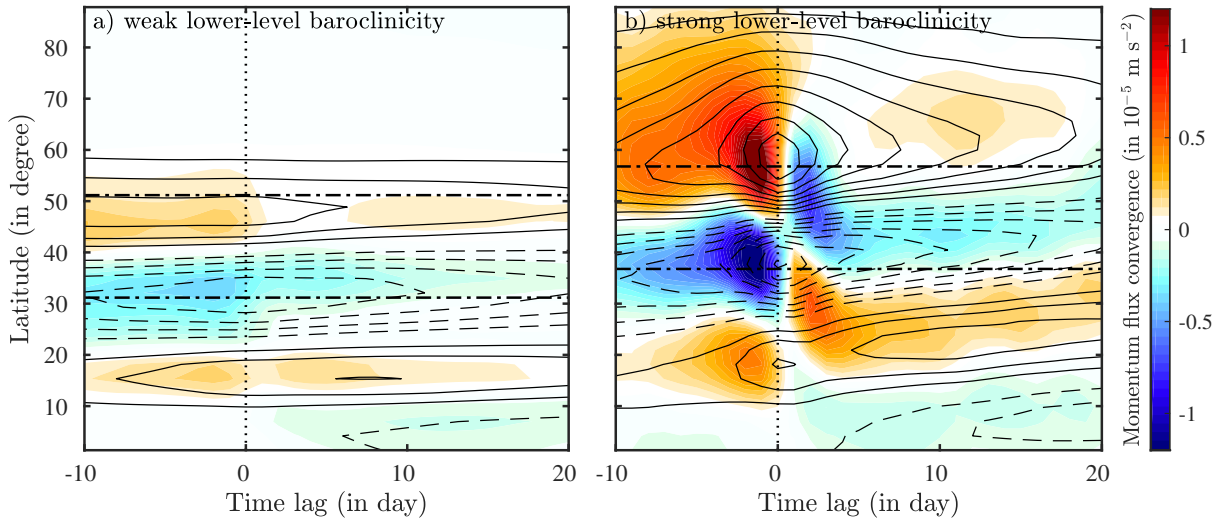




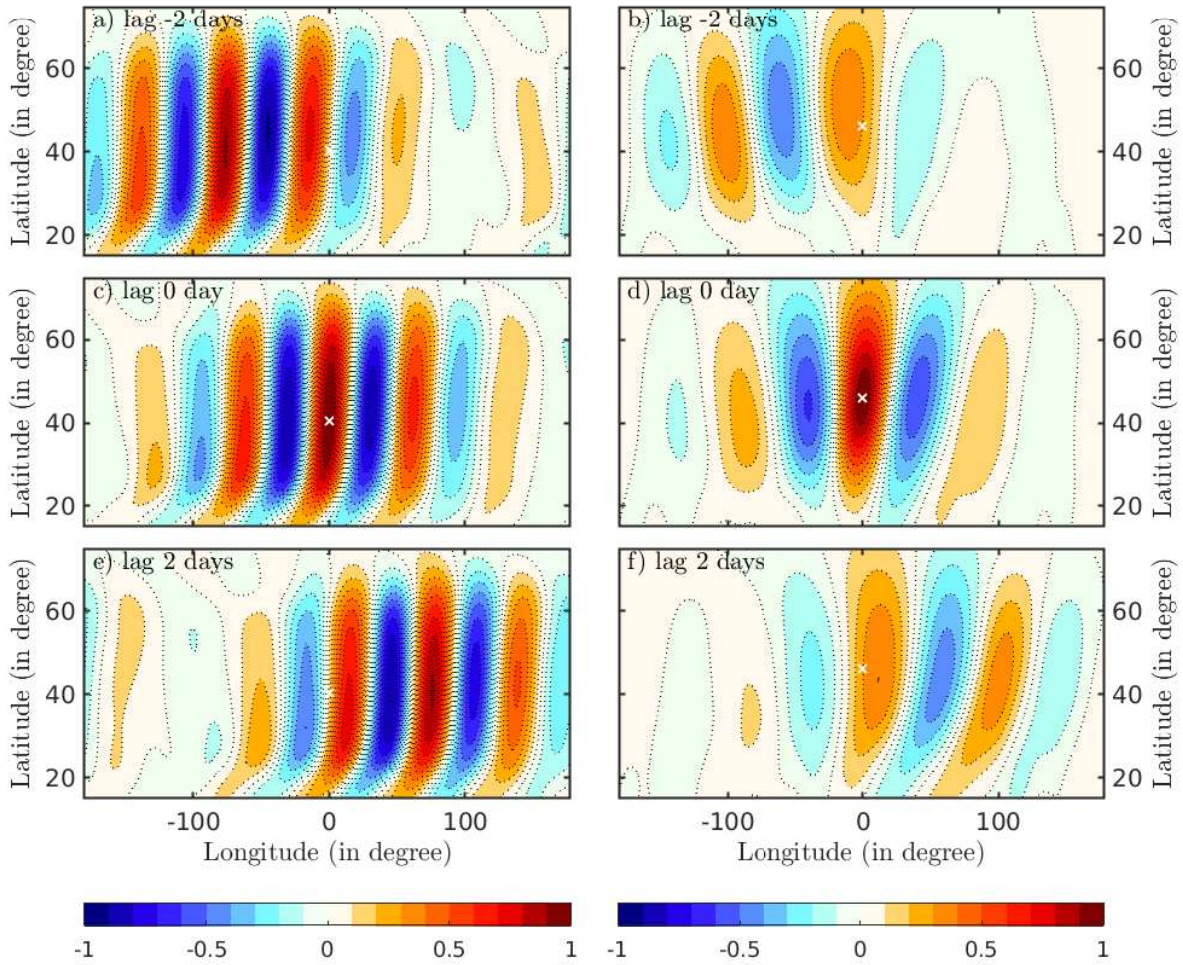
581 FIG. 3. eddy momentum contribution to the rate of change of the PC1 autocorrelation function ( $\tau_m^{-1}$  of  
 582 Eq. (5)), as a function of lag and baroclinicity factors for (a) UB25 and (b) LB25. The baroclinicity factors in  
 583 (a) and (b) correspond to  $(U_1 - U_2)/U_0$  and  $(U_2 - U_3)/U_0$  respectively.



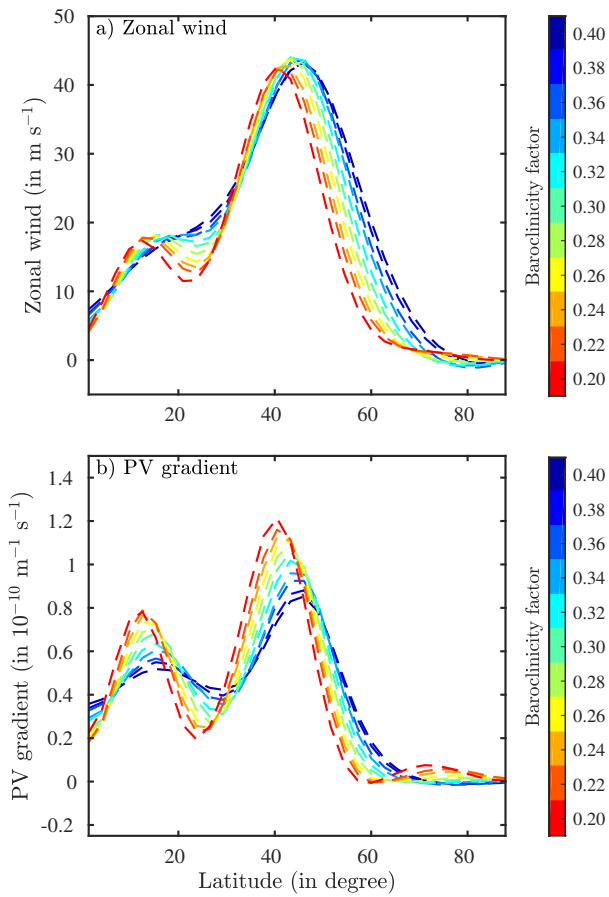
584 FIG. 4. Rate of change of the PC1 autocorrelation function (left-hand-side of Eq. (5)), in green), and its  
 585 momentum ( $\tau_m^{-1}$  of Eq. (5), in black) and drag contribution ( $\tau_m^{-1}$  of Eq. (5), in blue), for two simulations of  
 586 LB25 : (a) weak baroclinicity ( $U_2 - U_3 = 0.2U_0$ ) and (b) strong baroclinicity ( $U_2 - U_3 = 0.4U_0$ ).



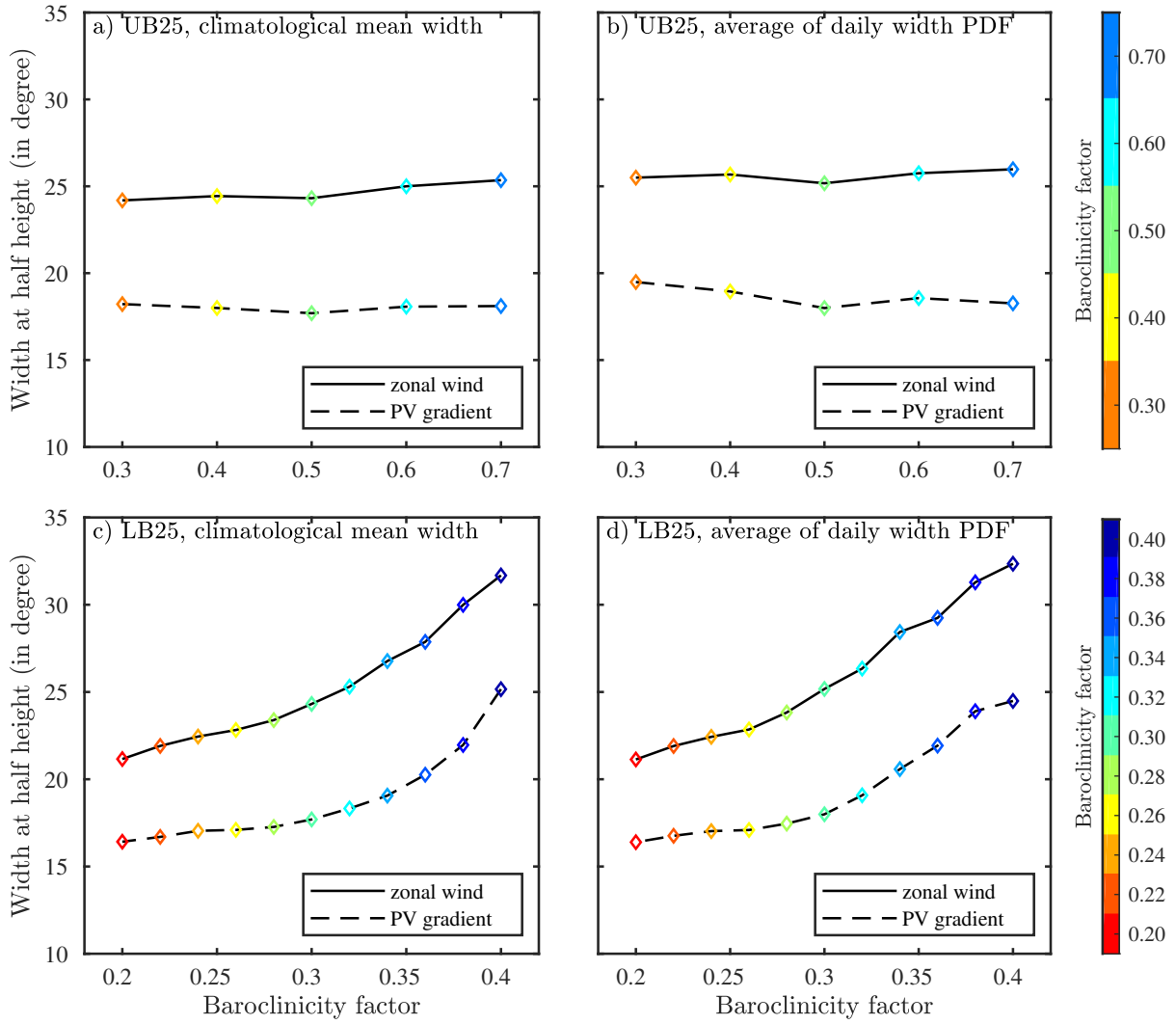
587 FIG. 5. Lagged regression onto PC1 of anomalous zonally and vertically-averaged eddy momentum flux  
 588 convergence (in shading) and zonal wind (in contours, interval:  $0.5 \text{ m s}^{-1}$ ) as a function of lag and latitude for  
 589 two simulations of LB25 : (a) weak baroclinicity ( $U_2 - U_3 = 0.2U_0$ ) and (b) strong baroclinicity ( $U_2 - U_3 =$   
 590  $0.4U_0$ ). The black dashed-dotted lines indicate the meridional extension of the mean jet (taken as  $\pm 10^\circ$  around  
 591 jet maximum).



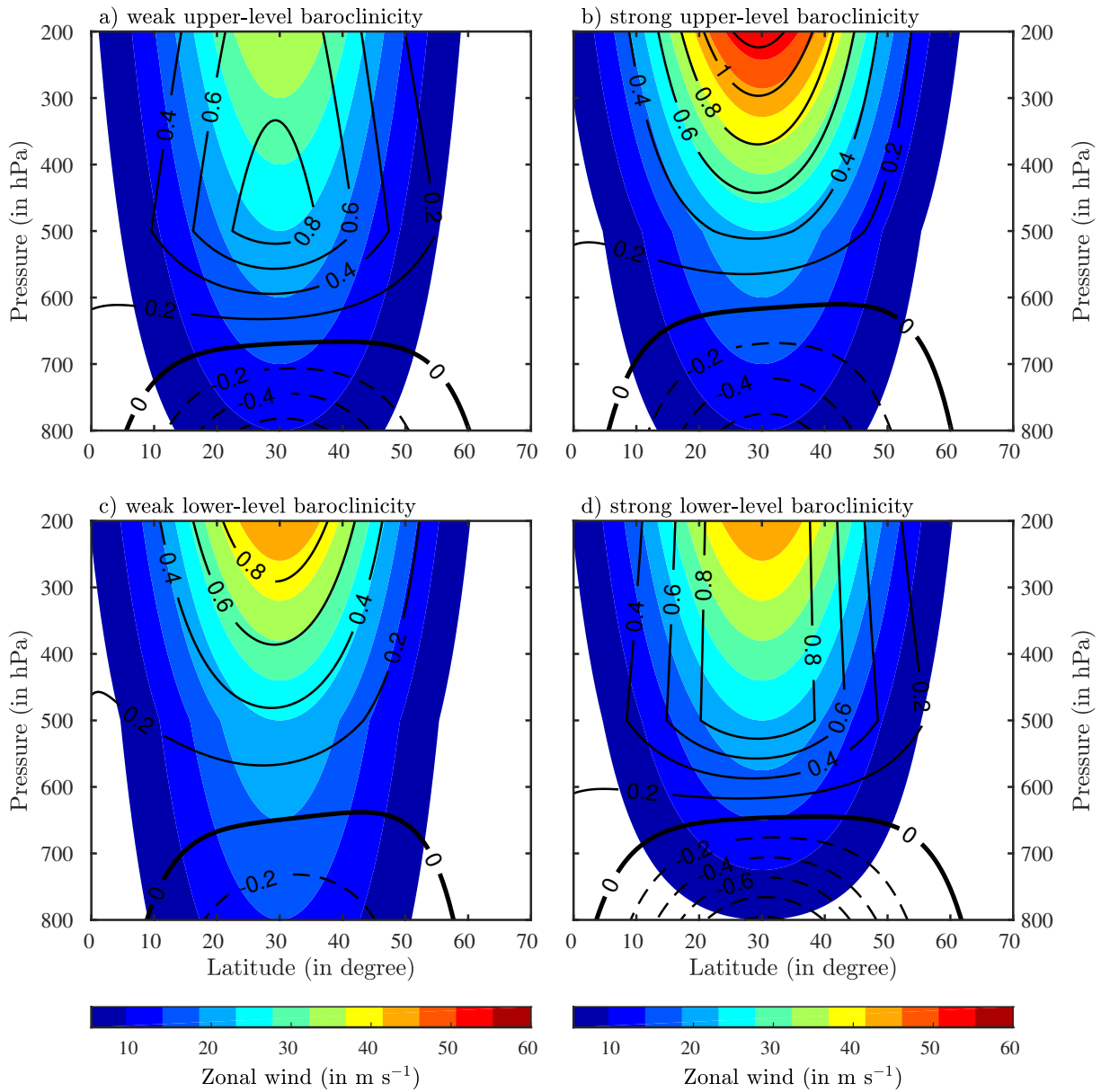
592 FIG. 6. Lagged one point correlation map of the meridional wind for (left panels) weak lower-level baroclin-  
 593 icity ( $U_2 - U_3 = 0.2U_0$ ) and (right panels) strong lower-level baroclinicity ( $U_2 - U_3 = 0.4U_0$ ). These correlations  
 594 maps have been plotted with a lag of (a,b) -2 days, (c,d) 0 day and (e,f) +2 days. The reference point, plotted  
 595 using a white cross, is in each simulation close to the maximum of zonal wind.



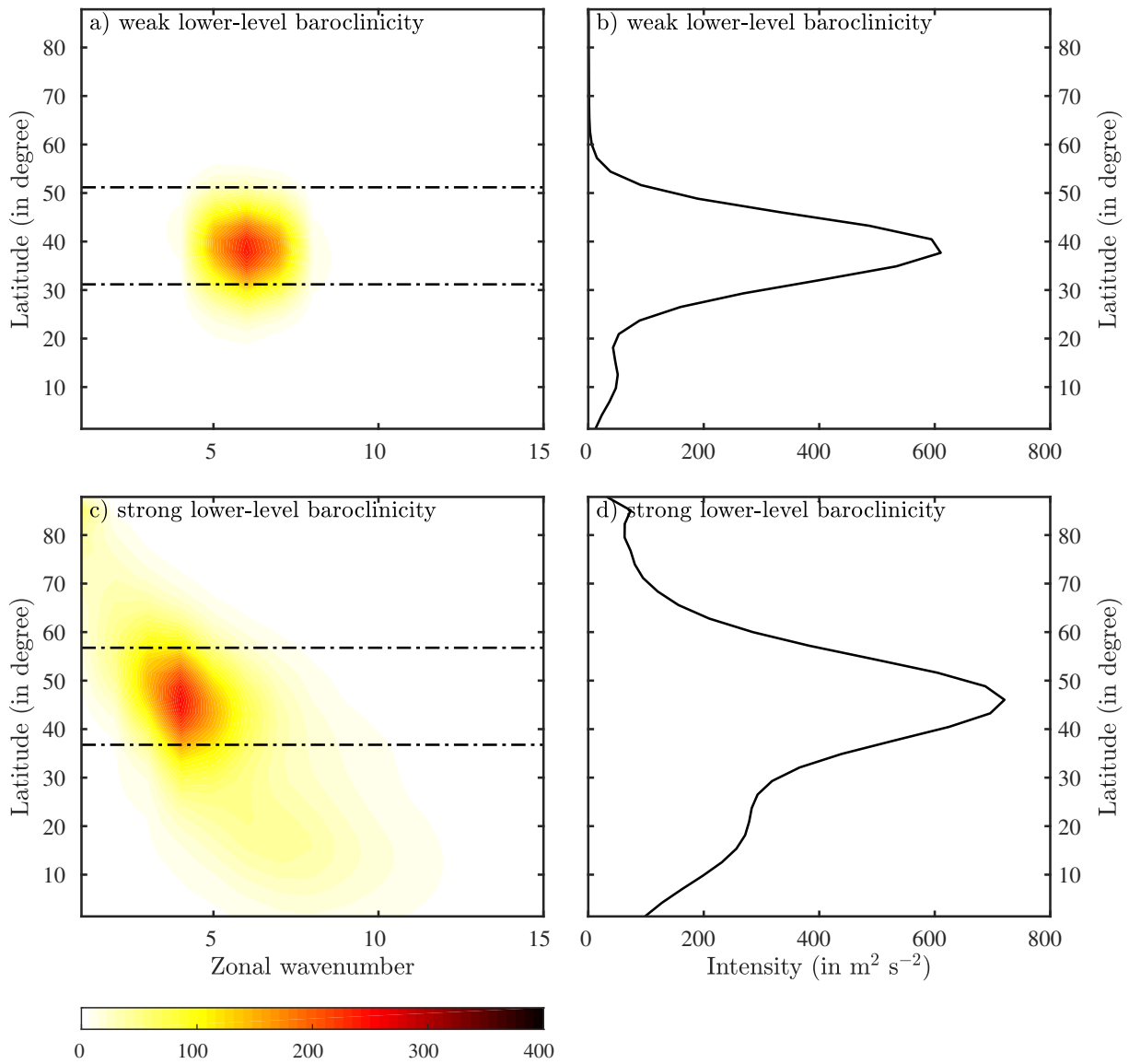
596 FIG. 7. Climatological mean of (a) the zonally averaged zonal wind and (b) zonally averaged PV gradient at  
 597 200hPa for LB25, the baroclinicity factor being  $(U_2 - U_3)/U_0$ .



598 FIG. 8. (a,c) Full width at half maximum of the main peak of zonally averaged zonal wind (solid line) and  
 599 PV gradient (dashed line) at 200hPa and (b,d) averaged full width at half maximum of the daily peak of the  
 600 same quantities as a function of (a,b) the upper-level baroclinicity factor  $(U_1 - U_2)/U_0$  for each simulation of  
 601 UB25 and (c,d) the lower-level baroclinicity factor  $(U_2 - U_3)/U_0$  for each simulation of LB25 (plotted with their  
 602 respective color).

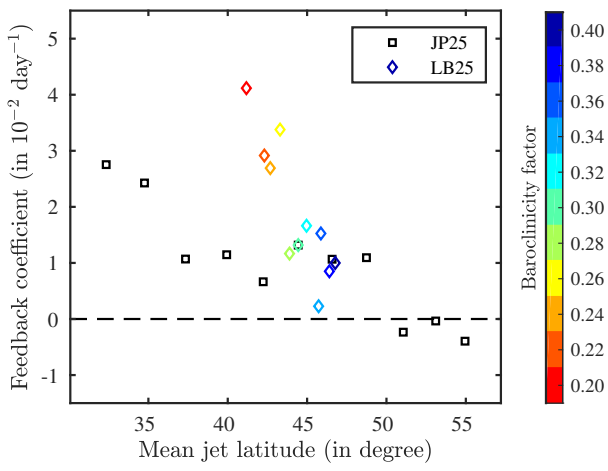


603 FIG. 9. Vertical cross-section of the zonal wind (in shadings) and PV gradient (in contours, interval:  
 604  $2 \cdot 10^{-11} \text{ m}^{-1} \text{ s}^{-1}$ ) of the restoration basic states for (a) weak upper-level baroclinicity ( $U_1 - U_2 = 0.4U_0$ ), (b)  
 605 strong upper-level baroclinicity ( $U_1 - U_2 = 0.7U_0$ ), (c) weak lower-level baroclinicity ( $U_2 - U_3 = 0.2U_0$ ) and (d)  
 606 strong lower-level baroclinicity ( $U_2 - U_3 = 0.4U_0$ ).



607 FIG. 10. (a,c) Spectrum of the squared meridional wind as a function of latitude and zonal wave number and  
 608 (b,d) its integral over wavenumber for (a,b) a weak lower-level baroclinicity ( $U_2 - U_3 = 0.2U_0$ ) and (c,d) a strong  
 609 lower-level baroclinicity ( $U_2 - U_3 = 0.4U_0$ ).





610 FIG. 11. Feedback coefficient as a function of mean jet position for the JP25 series (in black squares) and the  
 611 LB25 series (in colored diamonds), the baroclinicity factor being  $(U_2 - U_3)/U_0$ .

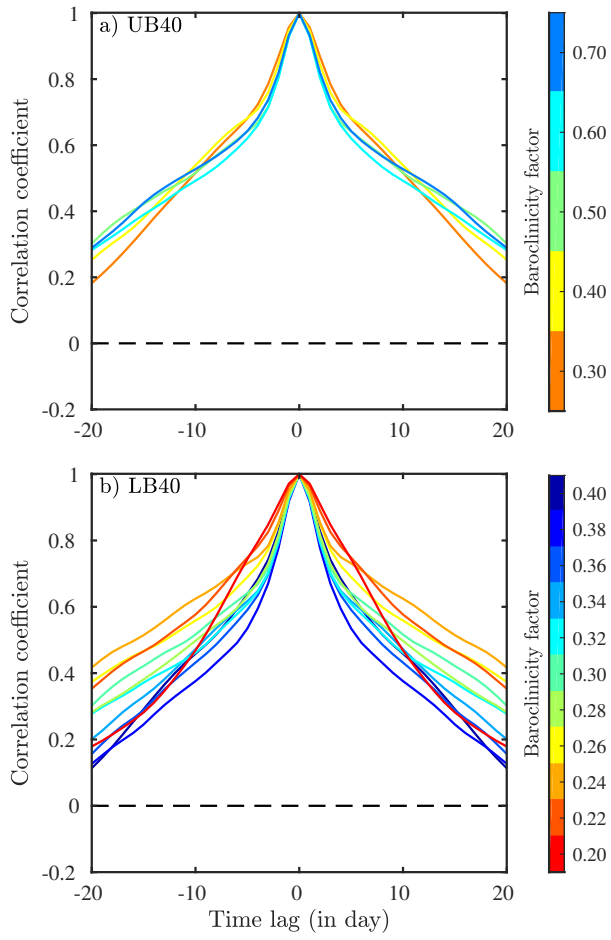


FIG. 12. As Fig. 2 but for UB40 and LB40 series.

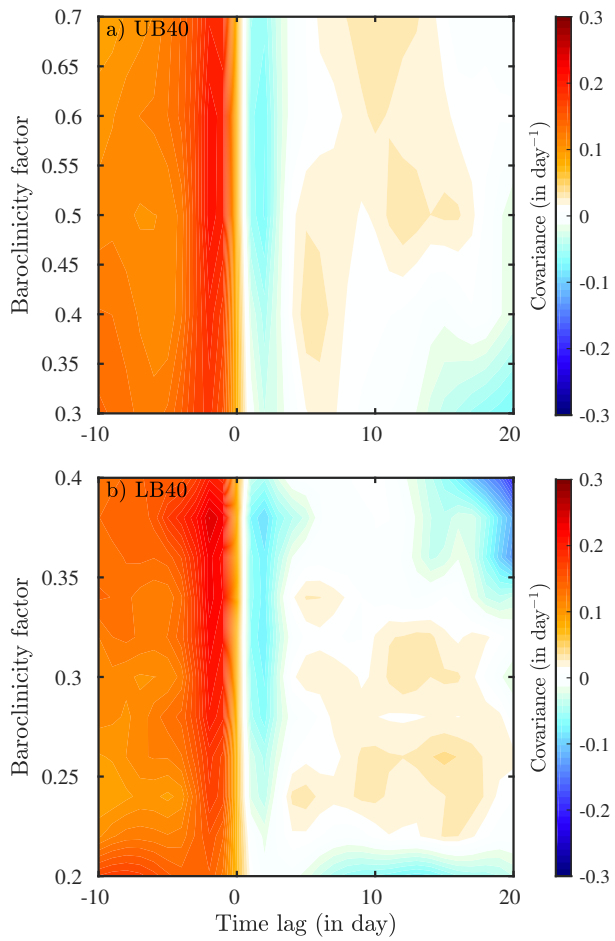


FIG. 13. As Fig. 3 but for UB40 and LB40 series.